



Effect of ferromagnetic exchange field on band gap and spin polarisation of graphene on a TMD substrate

PARTHA GOSWAMI

Physics Department, D.B. College, University of Delhi, Kalkaji, New Delhi 110 019, India
E-mail: physicsgoswami@gmail.com

MS received 31 August 2016; revised 23 July 2017; accepted 26 September 2017;
published online 19 February 2018

Abstract. We calculate the electronic band dispersion of graphene monolayer on a two-dimensional transition metal dichalcogenide substrate (GrTMD) around \mathbf{K} and \mathbf{K}' points by taking into account the interplay of the ferromagnetic impurities and the substrate-induced interactions. The latter are (strongly enhanced) intrinsic spin-orbit interaction (SOI), the extrinsic Rashba spin-orbit interaction (RSOI) and the one related to the transfer of the electronic charge from graphene to substrate. We introduce exchange field (M) in the Hamiltonian to take into account the deposition of magnetic impurities on the graphene surface. The cavalcade of the perturbations yield particle-hole symmetric band dispersion with an effective Zeeman field due to the interplay of the substrate-induced interactions with RSOI as the prime player. Our graphical analysis with extremely low-lying states strongly suggests the following: The GrTMDs, such as graphene on WY_2 , exhibit (direct) band-gap narrowing/widening (Moss-Burstein (MB) gap shift) including the increase in spin polarisation (P) at low temperature due to the increase in the exchange field (M) at the Dirac points. The polarisation is found to be electric field tunable as well. Finally, there is anticrossing of non-parabolic bands with opposite spins, the gap closing with same spins, etc. around the Dirac points. A direct electric field control of magnetism at the nanoscale is needed here. The magnetic multiferroics, like BiFeO_3 (BFO), are useful for this purpose due to the coupling between the magnetic and electric order parameters.

Keywords. Transition metal dichalcogenides; band dispersion; exchange field; low-lying states; Moss-Burstein shift.

PACS Nos 73.22.-f; 73.43.-f; 72.80.Vp; 73.63.-b; 72.20.-i

1. Introduction

The theoretical and the experimental investigations in material science took a completely different turn ever since graphene was isolated and produced in 2004 [1,2]. Despite its remarkable properties [3,4], it has not been possible to fully exploit its potential due to the difficulty of opening a reasonably sized gap in its band structure. As a result, the attention of the material science community had begun to shift to other two-dimensional (2D) systems such as transition metal dichalcogenides (TMD) (such as $\text{WSe}_2/\text{WS}_2/\text{MoSe}_2/\text{MoS}_2$) [5–7], phosphorene [8], silicene [9], and lately on hexagonal monolayers made up of group IV and VI elements [10–13], viz. SnS, SnSe, GeS, GeSe, etc. The hunt for the new 2D materials is on.

The silicene (Si monolayer with buckled structure) and phosphorene (phosphorus monolayer with puckered structure) have opened up the possibility of the

use of group IV/V based 2D materials for electronics applications [9,14–17]. The silicene allows creation of an electric-field tunable band gap, but like graphene it is a better conductor of electrons than most of the TMDs. Moreover, the instability and the reactivity of a monolayer silicene in air is phenomenally high. Thus, it fails to act as an appropriate platform for the digital electronics. Interestingly, phosphorene has an inherent, direct and appreciable band gap that depends on the number of layers. It is shown to act as a field effect transistor [17]. Though it is more stable than silicene, it, however, misses the appropriate platform mark as it also conducts electrons very swiftly. As regards {SnSe, GeS, ...}, these semiconducting materials undergo an indirect-to-direct gap transition by the application of mechanical strain and could be used as LEDs. Suggestion has come forth from several workers and collaborators [18] to combine these new 2D materials with known 2D materials in such a way that

all their different advantages are properly utilised in such structures. For example, the so-called van der Waals heterostructures (vdWHs) [19–23], assembled from atomically thin layers of graphene, hexagonal boron nitride and other related materials, have shown great potentials for band-structure engineering [24,25] of graphene. These novel structures not only offer a unique platform for the emerging devices with unprecedented functions, they also provide a fascinating dais for theoretical explorations through the handling of their confined electronic systems.

In this communication, we first introduce an enhanced spin–orbit interaction (SOI) in graphene on a 2D-TMD (GrTMD) substrate so that the resultant vdWH structure turns into a quantum spin-Hall (QSH) insulator [26,27]. In fact, Kane and Mele [27] were the first to suggest the existence of QSH effect for pure graphene when moderate to large SOI is taken into account. Recently, there have been reports of experimental observation of the SOI enhancement in graphene through the addition of SOI-active impurities [28]. In graphene and GrTMD, the effect of SOI is to create a bulk band gap. There is no parity exchange for the graphene system, as the relevant bands are all pi-bands with the same parity. Thus, no band inversion (BI) is possible. The absence of BI is unlike that in the Bernevig–Hughes–Zhang (BHZ) model [29], where the SOI induces BI at the high symmetry points in the Brillouin zone signaling the change in the parity of the valence-band-edge state and the transition from trivial to non-trivial insulator. As all time-reversal invariant insulators could be uniquely classified by the Z_2 topological invariant [27], the calculation of Z_2 for GrTMD system is required to ascertain its trivial/non-trivial topological nature. A confirmation of this must be sought by showing the existence of gapless edge states for wide ribbons of GrTMD as the QSH state is known to support [27,29] within the gap of a pair of counterpropagating spin-polarised edge modes. Relegating these issues, including the spin non-conservation due to Rashba spin–orbit interaction (RSOI), to a future publication, we exchange couple (M) the graphene layer in GrTMD system to localised magnetic impurities (MIs), such as substitutional Co atoms, breaking the time-reversal symmetry (TRS). This leads to the accessibility of the quantum anomalous Hall (QAH) state [30–32]. Our primary aim here is to investigate the band structure in QSH state ($M = 0$) and its evolution due to TRS breaking ($M \neq 0$). The problem is a novel one as the band structure evolution in the presence of such a large number of interactions is unknown. We start with an appropriate Hamiltonian [26,33–35] involving substrate-induced interactions (SIIs), viz. the much needed, enhanced sublattice-resolved intrinsic SOIs, the extrinsic RSOI and the orbital gap related to the transfer

of the electronic charge from graphene to the substrate for this purpose. The RSOI allows for external tuning of the band gap and connects the nearest neighbours with spin-flip. These four substrate-induced interaction terms, shown in figure 1, are time-reversal invariant and absent by inversion symmetry in isolated pristine, pure graphene monolayer. There are two distinct systems in the presence of MIs, viz. AA (when the magnetic impurities are located in the same sublattice) and AB (when the impurities are in opposite sublattices) [36–38]. We calculate the band structure and the spin polarisation of these systems as a function of magnetisation strength. We also discuss the valley-polarisation and line defect [39,40] in brief at the end. The interplay of SIIs, together with coupling between an impurity moment and GrTMD itinerant electrons and the line defect are expected to show the efficacious route to tune the spin-valley electronic properties of graphene.

The SIIs lead to spin-valley resolved bands of the form $\varepsilon_{\xi,s,\sigma}(k, M) = [sP(k, M, \xi) + \sigma\sqrt{\varepsilon_k^2 + Q^2(k, M, s, \xi)}]$. For the two systems, the functions (P, Q) are different. The band structure corresponds to QSH and QAH for $M = 0$ and $M \neq 0$, respectively. It consists of two spin-chiral conduction bands and two spin-chiral valence bands. Because of the spin-mixing driven by the Rashba coupling, the spin is no longer a

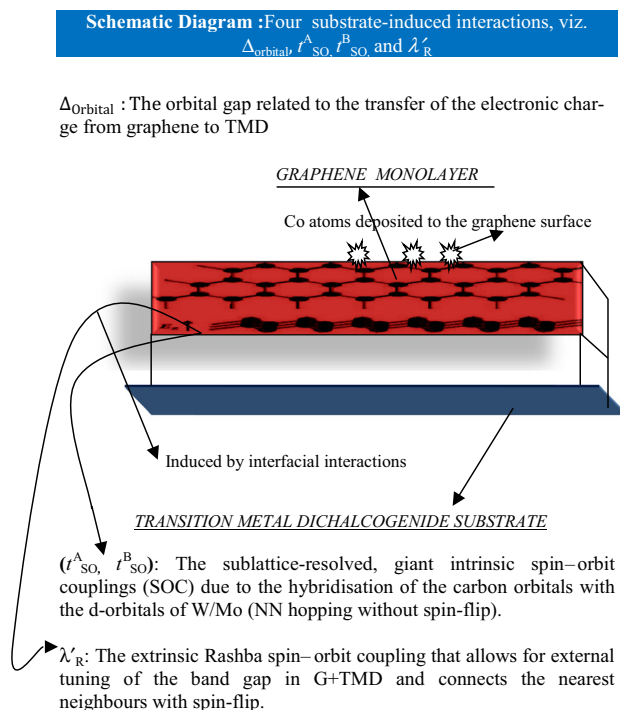


Figure 1. A schematic diagram of the graphene on two-dimensional TMD. The four substrate-induced interaction terms, $\Delta_{\text{orbital}}, t_{\text{SO}}^A, t_{\text{SO}}^B$, and λ'_R , shown in the figure, are time-reversal invariant and are absent by inversion symmetry in isolated pristine, pure graphene sheets.

good quantum number. Therefore, the resulting angular momentum eigenstates may be denoted by the spin-chirality index $s = \pm 1$. Here, $\sigma = + (-)$ indicates the conduction (valence) band and $\xi = +1 (\xi = -1)$ the Dirac point $\mathbf{K} (\mathbf{K}')$; ε_k is the spin-valley degenerate energy dispersion of the pristine, pure graphene. We shall see that $P(k, M, \xi) = P(-k, M, \xi)$ and $Q(k, M, s, \xi) = Q(-k, M, s, \xi) \neq Q(-k, M, -s, \xi)$. The band structure (i) preserves the inversion symmetry ($\varepsilon_{\xi,s,\sigma}(k, M) = \varepsilon_{\xi,s,\sigma}(-k, M)$), (ii) breaks the TRS ($\varepsilon_{\xi,s,\sigma}(k, M) \neq \varepsilon_{\xi,-s,\sigma}(-k, M)$), (iii) involves an effective Zeeman field $P(k, M, \xi)$ due to the interplay of the substrate-induced interactions (This term vanishes for the AA system if the magnitude of the SOIs are assumed to be equal. For the AB system, apart from this equality, one should have $M = 0$.), (iv) involves the spin-orbit interaction led avoided crossing of the bands with the same spins around Dirac points (see figure 3a), (v) the band-gap narrowing/widening (for a certain range of exchange field values) due to the presence of the exchange field (see figures 3a–3c), (vi) exhibits the inversion of the two valence bands with the swapped spin states at $M = M_{bi}$ (a critical value) (see figure 3d), and so on. The anticrossing of the non-parabolic bands have been shown by Tse *et al* [41] several years ago. As the rest of the findings are novel ones for the GrTMD system, our discussion will be centred around the same. On a quick side note, the present work is motivated by a series of theoretical investigations on the same system by Gmitra *et al* [26,33–35]. The experimental finding of a gap of 0.26 eV when graphene is epitaxially grown on the SiC substrate [32] is another motivating result which gives justification of considering a substrate-induced interaction and the corresponding gap Δ_{orbital} . This gap increases as the sample thickness decreases. It has been proposed that the origin of this gap is the breaking of sublattice

symmetry owing to the graphene–substrate interaction. A direct, functional electric field control of magnetism at the nanoscale is needed for the effective demonstration of our results. The magnetic multiferroics, like BiFeO₃ (BFO), have piqued the interest of the researchers world-wide with the promise of the coupling between the magnetic and electric order parameters.

The paper is organised as follows: In §2, a brief outline of the low-energy model of GrTMD, involving exchange interaction (M) due to the proximity effect of the magnetic impurities introduced, is given and the single-particle excitation spectrum is obtained. The spectrum is obtained from a quartic, involving all the substrate-induced perturbations. Our calculations relating to the effect of M on the band gap, are presented in §3. The spin polarisation due to M has also been examined in this section. The paper ends with brief discussion and concluding remarks.

2. Hamiltonian of graphene on TMD substrate

We consider the detailed Hamiltonian [26,33–35] of GrTMD built on the orbital Hamiltonian for pristine graphene. The detailed Hamiltonian is basically a low-energy one around the Dirac points \mathbf{K} and \mathbf{K}' in the basis $(a_{\mathbf{k}\uparrow}^\xi, b_{\mathbf{k}\downarrow}^\xi, a_{\mathbf{k}\downarrow}^\xi, b_{\mathbf{k}\uparrow}^\xi)$ in momentum space. Here, $a_{\mathbf{k}\sigma}^\xi (b_{\mathbf{k}\sigma}^\xi)$ is the fermion annihilation operator for the state (\mathbf{k}, σ) corresponding to the valley $\xi = \pm 1$, and the sublattice A(B). The Hamiltonian consists of all the four SIIs mentioned above. The SIIs are time-reversal invariant and absent by inversion symmetry in isolated graphene sheets. Therefore, the low-energy dimensionless Hamiltonian [26,33–35] for a GrTMD system, where the nearest neighbour hopping is parametrised by a hybridisation t , is written as

$$H / \left(\frac{\hbar v_F}{a} \right) = \sum_{\delta \mathbf{k}} (a_{\delta \mathbf{k}\uparrow}^{\dagger \xi} b_{\delta \mathbf{k}\downarrow}^{\dagger \xi} a_{\delta \mathbf{k}\downarrow}^{\dagger \xi} b_{\delta \mathbf{k}\uparrow}^{\dagger \xi}) \frac{\mathbb{H}(\delta \mathbf{k})}{\left(\frac{\hbar v_F}{a} \right)} \begin{pmatrix} a_{\delta \mathbf{k}\uparrow}^\xi \\ b_{\delta \mathbf{k}\downarrow}^\xi \\ a_{\delta \mathbf{k}\downarrow}^\xi \\ b_{\delta \mathbf{k}\uparrow}^\xi \end{pmatrix} \quad (1)$$

$$\frac{\mathbb{H}(\delta \mathbf{k})}{(\hbar v_F/a)} = \begin{pmatrix} a_1 & h_+^\xi & -(\lambda^+ + \lambda^-) ia\delta \mathbf{k}_- & -a\delta \mathbf{k}_+^\xi \\ h_+^{\xi*} & a_2 & -a\delta \mathbf{k}_-^\xi & -(\lambda^+ - \lambda^-) ia\delta \mathbf{k}_+ \\ (\lambda^+ + \lambda^-) ia\delta \mathbf{k}_+ & -a\delta \mathbf{k}_+^\xi & a_3 & h_-^\xi \\ -a\delta \mathbf{k}_-^\xi & (\lambda^+ - \lambda^-) ia\delta \mathbf{k}_- & h_-^{\xi*} & a_4 \end{pmatrix} \quad (2)$$

$$a_1 = \Delta + M + \xi \Delta_{\text{soc}}^A, \quad a_2 = -\Delta \mp M + \xi \Delta_{\text{soc}}^B, \quad a_3 = \Delta - M - \xi \Delta_{\text{soc}}^A, \\ a_4 = -\Delta \pm M - \xi \Delta_{\text{soc}}^B, \quad h_+^\xi = \frac{3}{2} i \lambda_R(E) (1 + \xi), \quad h_-^\xi = \frac{3}{2} i \lambda_R(E) (1 - \xi). \quad (3)$$

Table 1. Values of the orbital and spin-orbital parameters.

TMD	t (eV)	Δ_{Orbital} (meV)	t_{so}^{A} (meV)	t_{so}^{B} (meV)	λ'_{R} (meV)
WSe ₂	2.51	0.54	−1.22	1.16	0.56
WS ₂	2.66	1.31	−1.02	1.21	0.36
MoSe ₂	2.53	0.44	−0.19	0.16	0.26
MoS ₂	2.67	0.52	−0.23	0.28	0.13

Here $(\hbar v_F/a) = ((\sqrt{3}/2)t)$. In (a_1, a_2, a_3, a_4) the upper sign corresponds to the AA system and the lower one to AB, and $a = 2.46 \text{ \AA}$ is the pristine graphene lattice constant. Also, $\delta k_{\pm}^{\xi} \rightarrow \delta k_{\pm}$ (that is, $\delta k_x \pm i\delta k_y$) for the Dirac point \mathbf{K} ($\xi = +1$) and $\delta k_{\pm}^{\xi} \rightarrow \delta k_{\pm}^*$ (that is, $\delta k_x \mp i\delta k_y$) for the Dirac point \mathbf{K}' ($\xi = -1$). The quantity $E(s_z, t_z) = \xi t'_{\text{so}} s_z t_z + \Delta_z t_z + M s_z$, with the spin index $s_z = \pm 1$ and the sublattice pseudospin index $t_z = \pm 1$. The parameters' orbital proximity gap Δ , the intrinsic parameters $\Delta_{\text{soc}}^{\text{A}}$ and $\Delta_{\text{soc}}^{\text{B}}$ and the extrinsic Rashba parameter $\lambda_{\text{R}}(E_z)$ allow for tuning by the applied electric field. Since the WSe₂/MoS₂ layer provides different environment to atoms A and B in the graphene cell, there is this (dimensionless) orbital proximity gap $\Delta = \Delta_{\text{Orbital}}/(\hbar v_F/a)$ arising from the effective staggered potential induced by the pseudospin symmetry breaking. The orbital gap Δ_{Orbital} is about 0.5 meV [26,33–35] in the absence of electric field. When the field crosses a limiting value 0.5 V/nm, the gap exhibits a sharp increase. This gap is related to the transfer of the electronic charge occurring between graphene and the substrate. The TRS breaking could be accessed in GrTMD by introducing an exchange field. The exchange field M ($M = M'/(\hbar v_F/a)$) arises due to proximity coupling to magnetic impurities such as depositing Co atoms to the graphene surface. This modus operandi, to extract the exchange coupling effect, has been suggested in the case of graphene and silicene by several researchers [42–45]. Due to the hybridisation of the carbon orbitals with the d-orbitals of W/Mo, there is sublattice-resolved, giant intrinsic spin–orbit couplings ($t_{\text{so}}^{\text{A}}, t_{\text{so}}^{\text{B}}$)

$$\Delta_{\text{soc}}^{\text{A}} = \frac{t_{\text{so}}^{\text{A}}}{(\hbar v_F/a)}, \quad \Delta_{\text{soc}}^{\text{B}} = \frac{t_{\text{so}}^{\text{B}}}{(\hbar v_F/a)}.$$

These couplings correspond to next-nearest neighbour hopping [33–35] without spin-flip. The spin–orbit field parameter for GrTMD is about 0.50 meV, which is 20 times more than that in pure graphene [33–35] ($t_{\text{so}} \sim 24 \mu\text{eV}$). The parameter

$$\lambda_{\text{R}} = \lambda'_{\text{R}}/(\hbar v_F/a)$$

is the extrinsic Rashba spin–orbit coupling (RSOC), that allows for external tuning of the band gap in GrTMD and connects the nearest neighbours with spin-flip. It, thus, arises because the inversion symmetry is broken when graphene is placed on top of a TMD. While the intrinsic parameters $\Delta_{\text{soc}}^{\text{A}}$ and $\Delta_{\text{soc}}^{\text{B}}$ change rather moderately with the increase in the applied electric field, the Rashba parameter λ_{R} almost doubles in increasing the field from -2 to 2 V/nm. For the pristine graphene $\lambda'_{\text{R}} \approx 10 \mu\text{eV}$ whereas for GrTMD (WSe₂) it is 0.56 meV. Wang *et al* [35], however, have reported it to be approximately 1 meV. The spin-splitting by the Rashba term away from the points \mathbf{K} and \mathbf{K}' is the same as that at \mathbf{K} and \mathbf{K}' . The three spin–orbit interaction terms, with coupling constant ($t_{\text{so}}^{\text{A}}, t_{\text{so}}^{\text{B}}$) and λ'_{R} , are induced by interfacial interactions. Some of the values of the orbital and spin–orbital parameters are summarised in table 1. These parameters can be tuned by a transverse electric field and vertical strain. The sublattice-resolved, pseudospin inversion asymmetry-driven spin–orbit interaction term (ASOI), on the other hand, represents the next-nearest-neighbour, unlike the Rashba term, same sublattice hopping away from \mathbf{K} and \mathbf{K}' albeit with a spin flip. In the basis $(a_{\mathbf{k}\uparrow}^{\xi}, b_{\mathbf{k}\downarrow}^{\xi}, a_{\mathbf{k}\downarrow}^{\xi}, b_{\mathbf{k}\uparrow}^{\xi})$, the ASOI terms, involving

$$\lambda^{+} = \lambda'^{+}/\left(\frac{\hbar v_F}{a}\right), \quad \lambda^{-} = \lambda'^{-}/\left(\frac{\hbar v_F}{a}\right),$$

could be written in a manner as shown in, eq. (2). Here λ'^{+} and λ'^{-} , respectively, are the spin–orbit interactions representing the average coupling and the differential coupling between the A and B sublattices. We have not considered the intrinsic RSOI for the following reason: Unlike conventional semiconducting 2D electron gases, in which the Rashba coupling is modelled as $\alpha(\delta k_y \sigma_x - \delta k_x \sigma_y)$ where σ 's are the Pauli matrices, the Rashba coupling in graphene does not depend on the momentum. The reason is that Rashba coupling is proportional to velocity, which is constant for massless Dirac electrons in graphene.

The energy eigenvalues ($E(a|\delta\mathbf{k}|)$) of the matrix (2) are given by a quartic. In terms of the powers of ε (where $\varepsilon \equiv E(a|\delta\mathbf{k}|)/\lambda_{\text{R}}$), in the absence of PIA-driven terms,

the quartic may be written as $\varepsilon^4 - 2\varepsilon^2 b + b^2 = 4\varepsilon c + b^2 - d$, where

$$a = 0,$$

$$b_\xi(|\delta\mathbf{k}|, \xi, M) = \left[\left(\frac{\Delta}{\lambda_R} \right)^2 + \frac{\left(\frac{\Delta_{\text{soc}}^A}{\lambda_R} \right)^2 + \left(\frac{\Delta_{\text{soc}}^B}{\lambda_R} \right)^2}{2} + (9/4)(1 + \xi^2) + \left(\frac{M}{\lambda_R} \right)^2 + \left(\frac{\hbar v_F}{a} \right)^2 \left(\frac{a|\delta\mathbf{k}|^2}{\lambda_R'^2} \right) - \xi \left\{ \left(\frac{\Delta_{\text{soc}}^B}{\lambda_R} \right) + \left| \left(\frac{\Delta_{\text{soc}}^A}{\lambda_R} \right) \right| \right\} \left(\frac{M}{\lambda_R} \right) \right],$$

$$c_\xi(\xi, M) = \xi \left\{ \left(\frac{\Delta_{\text{soc}}^B}{\lambda_R} \right) - \left| \left(\frac{\Delta_{\text{soc}}^A}{\lambda_R} \right) \right| \right\} \left[\left(\frac{9}{4} \right) - \left(\frac{\Delta}{2\lambda_R} \right) \xi \left\{ \left(\frac{\Delta_{\text{soc}}^B}{\lambda_R} \right) + \left| \left(\frac{\Delta_{\text{soc}}^A}{\lambda_R} \right) \right| \right\} + \left(\frac{\Delta}{\lambda_R} \right) \left(\frac{M}{\lambda_R} \right) \right],$$

$$d_\xi(|\delta\mathbf{k}|, \xi, M) = \sum_{j=1}^5 d_j,$$

$$d_1 = \left\{ \left(\frac{\Delta}{\lambda_R} \right)^2 - \left(\xi \left(\frac{\Delta_{\text{soc}}^B}{\lambda_R} \right) - \left(\frac{M}{\lambda_R} \right) \right)^2 \right\} \times \left\{ \left(\frac{\Delta}{\lambda_R} \right)^2 - \left(\xi \left| \left(\frac{\Delta_{\text{soc}}^A}{\lambda_R} \right) \right| - \left(\frac{M}{\lambda_R} \right) \right)^2 \right\},$$

$$d_2 = (9/4)(1 + \xi)^2 \left[\left\{ \left(\frac{\Delta}{\lambda_R} \right) - \left(\frac{M}{\lambda_R} \right) \right\}^2 + \xi \left\{ \left(\frac{\Delta_{\text{soc}}^B}{\lambda_R} \right) + \left| \left(\frac{\Delta_{\text{soc}}^A}{\lambda_R} \right) \right| \right\} \left\{ \left(\frac{\Delta}{\lambda_R} \right) - \left(\frac{M}{\lambda_R} \right) \right\} + \left(\frac{\Delta_{\text{soc}}^B}{\lambda_R} \right) \left| \left(\frac{\Delta_{\text{soc}}^A}{\lambda_R} \right) \right| \right],$$

$$d_3 = (9/4)(1 - \xi)^2 \left[\left\{ \left(\frac{\Delta}{\lambda_R} \right) + \left(\frac{M}{\lambda_R} \right) \right\}^2 - \xi \left\{ \left(\frac{\Delta_{\text{soc}}^B}{\lambda_R} \right) + \left| \left(\frac{\Delta_{\text{soc}}^A}{\lambda_R} \right) \right| \right\} \left\{ \left(\frac{\Delta}{\lambda_R} \right) + \left(\frac{M}{\lambda_R} \right) \right\} + \left(\frac{\Delta_{\text{soc}}^B}{\lambda_R} \right) \left| \left(\frac{\Delta_{\text{soc}}^A}{\lambda_R} \right) \right| \right],$$

$$d_4 = \left(\frac{\hbar v_F}{a} \right)^2 \left(\frac{2(a|\delta\mathbf{k}|)^2}{\lambda_R'^2} \right) \left[\left\{ \left(\frac{\Delta}{\lambda_R} \right)^2 - \left(\frac{M}{\lambda_R} \right)^2 \right\} + \xi \left\{ \left(\frac{\Delta_{\text{soc}}^B}{\lambda_R} \right) + \left| \Delta_{\text{soc}}^A/\lambda_R \right| \right\} (M/\lambda_R) - \left(\left| \Delta_{\text{soc}}^A/\lambda_R \right| \right) \left(\Delta_{\text{soc}}^B/\lambda_R \right) \right],$$

$$d_5 = (\hbar v_F/a)^4 \left((a|\delta\mathbf{k}|)^4/\lambda_R'^2 \right). \quad (4)$$

We write $b(a|\delta\mathbf{k}|, \xi, M) = \varepsilon_{\delta k}^2 + \beta_\xi^2(M)$, where $\varepsilon_{\delta k}^2 = (\hbar v_F/a)^2((a|\delta\mathbf{k}|)^2/\lambda_R'^2)$ and

$$\beta_\xi^2(M) = [(\Delta/\lambda_R)^2 + (1/2)\{|\Delta_{\text{soc}}^A/\lambda_R|^2 + (\Delta_{\text{soc}}^B/\lambda_R)^2\} + (M/\lambda_R)^2 + (9/4)(1 + \xi^2) - \xi\{|\Delta_{\text{soc}}^A/\lambda_R| + (\Delta_{\text{soc}}^B/\lambda_R)\}(M/\lambda_R)]. \quad (5)$$

We now add and subtract an as yet unknown variable z within the squared term ($\varepsilon^4 - 2\varepsilon^2 b + b^2$):

$$(\varepsilon^2 - b + z - z)^2 = 4\varepsilon c + b^2 - d$$

or

$$(\varepsilon^2 - b + z)^2 = 2z\varepsilon^2 + 4\varepsilon c + (z^2 - 2bz + b^2 - d). \quad (6)$$

The relatively small term ($4\varepsilon c$) in eq. (6) vanishes if the magnitude of the sublattice-resolved SOIs are assumed to be equal. The necessity of retaining this term will be made clear shortly. We shall show that the term is responsible for the spin polarisation. Upon retaining the term ($4\varepsilon c$), eq. (6) or, the equation $\varepsilon^4 - 2\varepsilon^2 b - 4\varepsilon c + d = 0$ becomes evidently a quartic whereas ignoring it will give rise to a biquadratic with values of ε given by $\varepsilon^2 \approx b \pm \sqrt{b^2 - d}$. The left-hand side of (6) is a perfect square in the variable ε . This motivates us to rewrite the right-hand side in that form as well. Therefore, we require the discriminant of the quadratic in the variable ε to be zero. This yields $16c^2 - 8z(z^2 - 2bz + b^2 - d) = 0$ or,

$$z^3 - 2bz^2 + (b^2 - d)z - 2c^2 = 0. \quad (7)$$

The cubic equation above has the discriminant function

$$\aleph = 8b^3c^2 - 72bdc^2 + 4d(b^2 - d)^2 - 108c^4. \quad (8)$$

Since \aleph is positive as could be seen from figure 2a (we have plotted here \aleph as a function of M at a given $(a\delta k) = 0.001$ for graphene on WSe₂) we definitely have real roots of eq. (7). These roots, as functions of M , are shown in figure 2. The root corresponding to the uppermost line in figure 2b is the appropriate one as it is found to be real, rational and importantly, being of

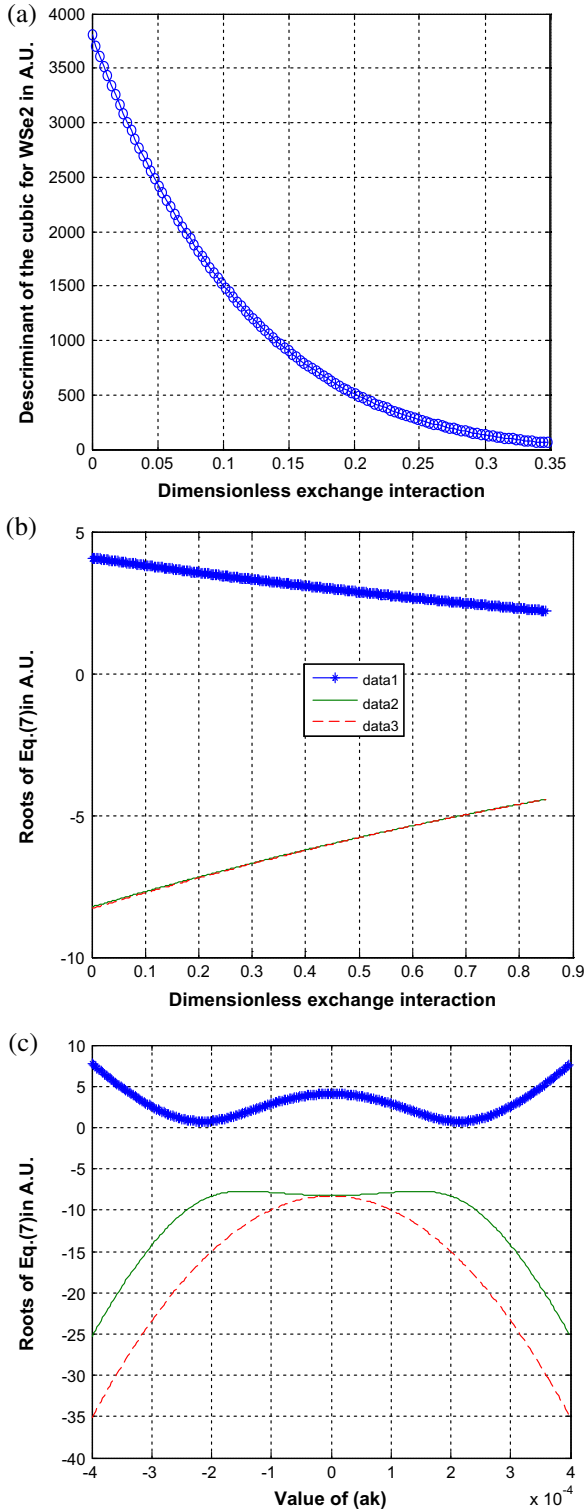


Figure 2. (a) A plot of the discriminant \aleph as a function of M . (b) The plots of the three (real and distinct) roots of (7) as functions of M . The uppermost curve (data 1) corresponds to the admissible roots as this is positive. (c) The plots of the three (real and distinct) roots of (7) as functions of $(a\delta\mathbf{k})$. The blue line corresponds to $z_0(a\delta\mathbf{k}, M)$. We find that $z_0(a\delta\mathbf{k}, M) = z_0(-a\delta\mathbf{k}, M)$.

positive sign yields real eigenvalues. Suppose we denote this root by $z_0(a\delta\mathbf{k}, \xi, M)$. We find that $z_0(a\delta\mathbf{k}, \xi, M) = z_0(-a\delta\mathbf{k}, \xi, M)$. Using (6) and (7) one may then write $\varepsilon^2 = b - z_0 \pm \{\sqrt{(2z_0)\varepsilon} + \sqrt{(2/z_0)c}\}$ or $\varepsilon^2 - \sqrt{(2z_0)\varepsilon} + (-b + z_0 - c\sqrt{(2/z_0)}) = 0$ and $\varepsilon^2 + \sqrt{(2z_0)\varepsilon} + (-b + z_0 + c\sqrt{(2/z_0)}) = 0$. These two equations basically yield the band structure

$$E_{\xi,s,\sigma,\delta k}(a|\delta\mathbf{k}|, M) = [s\sqrt{(z_0(a\delta\mathbf{k}, \xi, M)/2)\lambda_R} + \sigma\{(a|\delta\mathbf{k}|)^2 + \lambda_s(\xi, M)^2\}^{1/2}], \quad (9)$$

$$\lambda_s(\xi, M)^2 = \lambda_R^2\{\beta_\xi^2(M) - z_0/2 + s\sqrt{(2c_\xi^2(M)/z_0)}\}, \quad (10)$$

which consists of two spin chiral conduction bands and two spin chiral valence bands. The bands (in shorthand notation $E_{\xi,s,\sigma}(a|\delta\mathbf{k}|, M)$ – the energy eigenvalues of the matrix in eq. (2)) appear as spin-valley resolved and particle–hole symmetric as $z_0(a\delta\mathbf{k}, M) = z_0(-a\delta\mathbf{k}, M)$. There is an effective Zeeman field ($s\sqrt{(z_0/2)\lambda_R}$) in eq. (9) due to the interplay of the substrate-induced interactions. This term is an outcome of retaining the relatively small ($4\varepsilon c$) in eq. (6). Without this the discussion on spin polarisation remains incomplete. As could be seen from table 1, the sum of the absolute value of the intrinsic SOI terms is greater than the term Δ_{Orbital} characterising the (staggered) sublattice asymmetry in the graphene A and B atoms on WSe₂ and WS₂ whereas it is less for MoY₂. It is shown in figures 3a and 3f (see also ref. [46]) that as long as the former is valid the anticrossing of bands with opposite spins takes place around each of the valley near the \mathbf{K} point of graphene. However, when the latter is true, one makes a cross-over to a ‘direct half-metallic band’ regime with typically linear dispersion for the two opposite spin projections closer to zero energy (for MoSe₂ at the Dirac point \mathbf{K}). For the remaining two spin projections, there is anticrossing at the momentum (0, 0) indicated by oblique, intersecting lines. We now wish to describe the effect of the exchange field on the band gap. Corresponding to the AA system for graphene on WSe₂ at the Dirac point \mathbf{K} , we have shown a schematic band inversion between the two valence bands with opposite spin in figure 3d with the increase in the exchange interaction M . The trivial band gap (indicated by double arrow) between these two bands at $M = 0.00$ meV and $M = 0.50$ meV in figures 3a and 3b respectively closes at a critical point $M = M_c = 1.380$ meV in figure 3c, and reopens in figure 3d for $M = M_{bi} = 1.411$ meV exhibiting the inversion of these bands with the swapped spin states at $k = (0, 0)$. At $M > M_{bi}$ the energy eigenvalues are inadmissible as they become complex. In

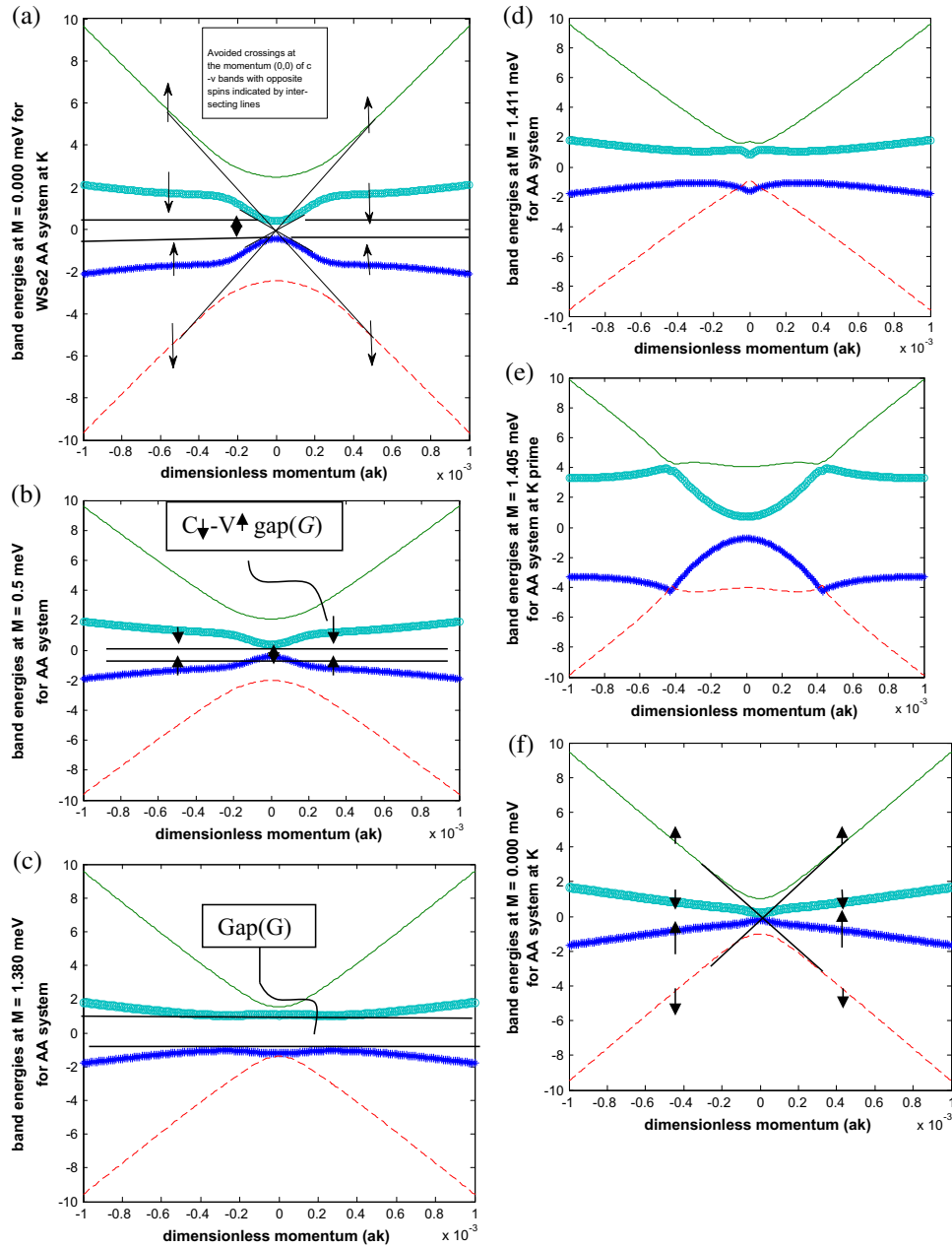


Figure 3. A schematic band inversion between two bands (valence bands with opposite spin) corresponding to the AA system for graphene in WSe₂ at the Dirac point **K**. The band identification is as follows: spin-up valence band: ‘- *’, spin-up conduction band: ‘-’, spin-down valence band: ‘- -’, and spin-down conduction band: ‘- o’. The trivial direct band gap (indicated by double arrow) between these two bands at $M = 0.00$ meV and $M = 0.50$ meV in (a) and (b) respectively closes at a critical point $M = M_c = 1.380$ meV in (c), and reopens at $M = M_{bi} = 1.411$ meV in (d) exhibiting the inversion of the two valence bands with the swapped spin states at $k = (0, 0)$. At $M > M_{bi}$ the energy eigenvalues are inadmissible as they become complex. As regards the band gap G between the down-spin conduction band and the spin-up valence band, it increases with M till M_c . (e) The band inversion taking place at $(0, \pm k_0)$ close to the Dirac point **K**’. (f) A cross-over to a ‘direct half-metallic band’ regime with typically linear dispersion for the two opposite spin projections closer to zero energy for MoSe₂ at the Dirac point **K**. For the remaining two spin projections, there is anticrossing at the momentum $(0, 0)$ indicated by oblique intersecting lines.

figure 3e we have shown that the band inversion takes place at $(0, \pm k_0)$ close to the Dirac point **K**’. Whether a band structure is wound up or not is a topological property, and one can measure it with topological indices

[47]. Now a topological insulator (TI) [47–49] exhibits a novel state that simultaneously possesses insulating bulk and conducting surface (edge) in one material. It is impossible to achieve this in conventional materials.

There are three keys to realise a TI: the TRS preservation, the SOI and the BI. For $M = 0$, TRS is unbroken in our system. In a future publication we shall report the calculation of the topological indices for the system at hand.

3. Spin polarisation

In the absence of the substrate-induced interactions and the exchange interactions, the band structure reduces to the spin-resolved, valley-degenerate energy dispersion of graphene, viz. $E_{\xi,s,\sigma}(a|\delta\mathbf{k}|, M) = [s\sqrt{(z_0/2)\lambda_R} + \sigma(a|\delta\mathbf{k}|)]$. If the RSOI is absent as well, then the band structure reduces to the spin-valley degenerate energy dispersion of the pristine, pure graphene: $e'_\sigma = \sigma(a|\delta\mathbf{k}|)$. It is gratifying to note that all the complexities present in the band structure is woven around the dispersion of pure graphene. Moving over to the energy bands, we find that the bands are strictly particle–hole symmetric despite retaining the term $(4\epsilon c)$ in eq. (6). The particle–hole symmetry in this context holds if we linearise the band structure near the Fermi level, so that filled states above the Fermi level and empty states below it have the same dispersion. The property to have the spectrum symmetry $\varepsilon_{\xi,s,\sigma}(a\delta\mathbf{k}, M) = \varepsilon_{\xi,s,\sigma}(-a\delta\mathbf{k}, M)$ is mandatory to have a particle–hole symmetry in this case. This is what is precisely not lacking in eq. (9), as $z_0(a\delta\mathbf{k}, \xi, M) = z_0(-a\delta\mathbf{k}, \xi, M)$. The meaning used here is different from the particle–hole (or charge conjugation) symmetry property of the mean-field theory of superconductivity where this property corresponds to an antiunitary operator involving the anticommutation of the Hamiltonian with the same.

The graphene on WS_2 and WSe_2 is gapped (with gap G) at all possible exchange field values (see figure 3) in our problem with a plethora of perturbations. On account of the strong spin–orbit coupling, the system acts as a QSH insulator for $M = 0$. As the exchange field (M) increases, the band-gap narrowing takes place followed by its recovery. The essential features of these curves, apart from the particle–hole symmetry, are (i) opening of an orbital gap due to the effective staggered potential, (ii) spin splitting of the bands due to the Rashba spin–orbit coupling and the exchange coupling and (iii) the band-gap narrowing and widening due to the many-body effect and the Moss–Burstein (MB) effect [50–52] respectively. The latter is due to the enhanced exchange effect. The exchange field M arises due to proximity coupling to ferromagnetic impurities. We consider the CV-direct band gap ($G_\xi(a|\delta\mathbf{k}|, M)$) for a given valley (see figures 3a–3c), i.e. the energy difference between the spin-down conduction band and the spin-up

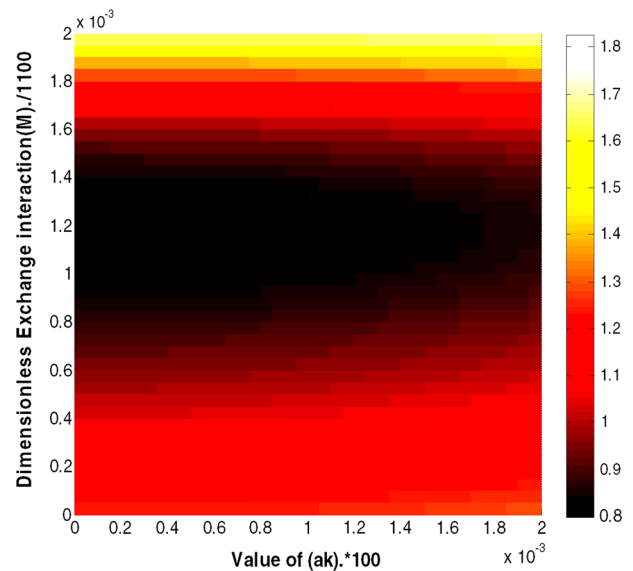


Figure 4. The contour plot of the relevant band gap as a function of the dimensionless wave vector and the exchange field (M) in the case of graphene on WSe_2 . This plot corroborates that, indeed, the band gap gets narrower followed by the gap recovery with the increase in the exchange field. The plots refer to the Dirac point \mathbf{K} .

valence band ($G_\xi(a|\delta\mathbf{k}|, M) = \varepsilon_{\xi,\downarrow,+1}(a|\delta\mathbf{k}|, M) - \varepsilon_{\xi,\uparrow,-1}(a|\delta\mathbf{k}|, M)$) to explain the MB effect. At the Dirac point \mathbf{K} , we find for WSe_2 that as the exchange field increases the CV-direct band gap between the spin-down conduction band and the spin-up valence band gets narrower followed by the gap recovery and the gap widening. The contour plot of this band gap in figure 4 as a function of the dimensionless wave vector and the exchange field (M) corroborates this fact. As regards MoY_2 , we find that there is Moss–Burstein (MB) shift only and no band narrowing. The shift due to the MB effect is usually observed due to the occupation of the higher energy levels in the conduction band from where the electron transition occurs instead of the conduction band minimum. On account of the MB effect, optical band gap is virtually shifted to high energies because of the high carrier density related band filling. This may occur with the elastic strain as well. Thus, studies are required to establish the simultaneous effect of the strain field and the carrier density on optical properties of GrTMD. We note that the band-gap narrowing and the v_F renormalisation, both in Dirac systems, are essentially many-body effects. Our observation of the gap narrowing in graphene on WSe_2 , thus, supports the hypothesis of v_F renormalisation [33]. Furthermore, (i) the direct information on the gap narrowing and the v_F renormalisation in graphene can be obtained from photoemission, which is a potent probe of many-body effects in solids

and (ii) as already mentioned, new mechanisms for achieving direct electric field control of ferromagnetism are highly desirable in the development of functional magnetic interfaces.

Moving over to eq. (9), we notice that RSOI ($\sqrt{(z_0/2)\lambda_R}$) here acts as an in-plane Zeeman term $g_b\mu_B B$ (where B is the magnetic field, g_b is the Lande g -factor and μ_B is the Bohr magneton). As already mentioned, the Zeeman term of the spectrum (9) comes into being due to the presence of the term ($4\epsilon c$) in (6). Without the term ($4\epsilon c$), the spectrum reduces to a biquadratic (with no Zeeman term) rather than a quartic. The Zeeman field, albeit the Rashba SOI with negligible orbital effects, in conjunction with the spin-orbit coupling (SOC), ushers in the spin polarisation to be explained below. For this purpose, we recall that the excess of one type of spin is given by $E = (n_\downarrow - n_\uparrow)/(n_\downarrow + n_\uparrow)$ where n_\uparrow (n_\downarrow) is the up (down)-spin carrier density. The spin polarisation (P), on the other hand, is defined in terms of the spin-dependent conductance G_s as $P = (G_\downarrow - G_\uparrow)/(G_\downarrow + G_\uparrow)$. The spin-dependent current density magnitude is $j_s = [(ev_F/A\pi) \sum_\xi \int_{\text{unfilled } \mathbf{k}} akd(ak) d(E_{\xi,s,\sigma=\pm 1,k}(a|\mathbf{k}|, M)/d(ak))]$ for an applied constant electric field which, in the Drude's picture, is proportional to the spin-dependent conductance. Here A is a characteristic area and a sum over states k is understood as an integral over all one-particle states. The contributions to the conductance from two Dirac nodes could be obtained by \sum_ξ . We next transform the momentum integral to an energy integral in the zero-temperature limit, though, admittedly, the finite-temperature limit would have been appropriate. We introduce the quantity $\mu' = \mu/(\hbar v_F/a)$ where μ is the dimensionless chemical potential of the fermion number. All states below μ are occupied. In view of eqs (9) and (10) we obtain $j_s \approx (e\mu'v_F/2A\pi) \sum_\xi [\eta\mu' - s\lambda_R\sqrt{(2z_0(0, \xi, M))}]$ where $\eta > 1$. We have approximated here $z_0(a\delta\mathbf{k}, \xi, M)$ by $z_0(0, \xi, M)$ and $\lambda_s(a\delta\mathbf{k}, \xi, M)$ by $\lambda_s(0, \xi, M)$ in view of their mild dependence on the wave vector. This immediately yields $P \sim (\lambda_R/\sqrt{2})[\sqrt{(z_0(\xi = +1, M))} + \sqrt{(z_0(\xi = -1, M))}]/\mu'$. The role of Rashba SOI as the polarisation-usher could be easily understood now. The polarisation (P) turns out to be electric field (E) tunable as λ_R is a function of E [26,33–35]. The plots of the spin polarisation (P) as a function of the exchange field in the case of graphene on WSe₂ for the AA system (blue curve) and AB system (green curve) at $T = 0$ K are shown in figure 5a. The plots indicate that the polarisation is exchange field (M) tunable, as there is an increase in P followed by a decrease when M increases. Since there is a general relation [53] between μ and V_g for a graphene-insulator-gate structure, viz. $\mu \approx \epsilon_a[(m^2 + 2eV_g/\epsilon_a)^{1/2} - m]$ where m is the

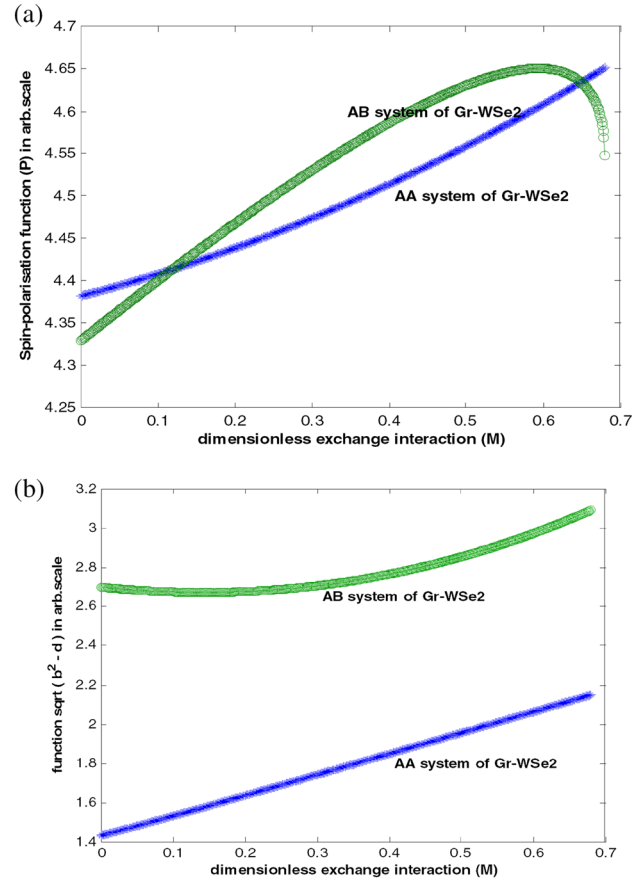


Figure 5. (a) The plots of the spin polarisation (P) as a function of the exchange field in the case of graphene on WSe₂ for the AA system (blue curve) and AB system (green curve) at $T = 0$ K. The plots indicate that, as M increases, there is a slight increase in P followed by a decrease. (b) The plots of $\sqrt{b_\xi^2(\delta k, M) - d_\xi(\delta k, M)}$ as a function of M for the AA system (blue curve) and AB system (green curve).

dimensionless ideality factor and ϵ_a is the characteristic energy scale, the tunability of P by the electrostatic doping is assured. Now the relation between μ and the carrier density may be given by $\mu \approx \hbar v_F \sqrt{(\pi|n|)\text{sgn}(n)}$ where $\text{sgn}(n) = \pm 1$ for the electron (hole) doping and n is the carrier concentration, and we obtain $P \sim n^{-1/2}$. Note that P has opposite signs for the electron and hole doping. As we have $z_0(\xi, M) \approx \lambda_R^2 [b_\xi(\xi, M) + \sqrt{d_\xi(\xi, M)}]$ from eq. (7), where (b_ξ, d_ξ) are given by eq. (4), the dependence of the spin polarisation on SII parameters, such as the intrinsic SOI, orbital gap, etc., is also obvious. The dependence on intrinsic SOI is easy to understand in a qualitative way: We recall that spin-orbit coupling is the natural outcome of incorporating special relativity within quantum mechanics. The external electric field along with that from the atomic cores is Lorentz-transformed into an effective magnetic field in the rest frame of an electron moving through a lattice. This effective field, subsequently,

acts upon the spin of the electron. It may be mentioned that the spin–orbit interaction utilisation for manipulating the electron spin has several distinct advantages, such as, the obviation of the design complexities that are often associated with incorporating local magnetic fields into a device architecture. The polarised electron spins in graphene may be probed through their interaction with optical fields. The polarisation of light incident on graphene will rotate in proportion to the strength of the magnetic field produced by this spin polarisation. The rotation is known as the Faraday (Kerr) effect in transmission (reflection). The spin–orbit coupling generates spin polarisation through yet another route: the (spin-dependent) skew scattering of relativistic electrons by a Coulomb potential in which electrons with spin-up and spin-down are scattered in opposite trajectories [50]. The extensive investigation of these issues, however, has been relegated to a future communication.

Table 1 shows that $(\Delta_{\text{soc}}^{\text{B}}/\lambda_{\text{R}})$ is approximately equal to the absolute magnitude of $(\Delta_{\text{soc}}^{\text{A}}/\lambda_{\text{R}})$ in all the cases, viz. those of MoS_2 , MoSe_2 , WS_2 and WSe_2 . As a result, in the equation $\varepsilon^4 - 2\varepsilon^2 b - 4\varepsilon c + d = 0$, one may be tempted to ignore the term $(4\varepsilon c) \sim \{(|\Delta_{\text{soc}}^{\text{A}}/\lambda_{\text{R}}|) - (\Delta_{\text{soc}}^{\text{B}}/\lambda_{\text{R}})\}\{..\}$ compared to the other terms. Ignoring the term $(4\varepsilon c)$ simply means the magnitudes of the sublattice-resolved SOCs are nearly equal, i.e. $|\Delta_{\text{soc}}^{\text{A}}/\lambda_{\text{R}}| \approx (\Delta_{\text{soc}}^{\text{B}}/\lambda_{\text{R}}) = (\Delta_{\text{soc}}/\lambda_{\text{R}})$. Thus, we have a biquadratic in place of a quartic. This immediately yields $\varepsilon^2 \approx b + s\sqrt{(b^2 - d)}$. We now write the typical particle–hole symmetric band structure $\varepsilon(\delta k, M)$, arising out of $\varepsilon^2 \approx b + s\sqrt{(b^2 - d)}$ and which consists of two spin-chiral conduction and two spin-chiral valence bands, as

$$\varepsilon(\delta k, M) = \sigma[\varepsilon_{\delta k}^2 + \Delta_{\xi, s}^2(\delta k, M)]^{1/2}$$

where

$$\begin{aligned} \varepsilon_{\delta k}^2 &= (\hbar v_F/a)^2((a|\delta \mathbf{k}|)^2/\lambda_{\text{R}}^2), \\ \Delta_{\xi, s}^2(\delta k, M) &= [(\Delta/\lambda_{\text{R}})^2 + (\Delta_{\text{soc}}/\lambda_{\text{R}})^2 + (M/\lambda_{\text{R}})^2 \\ &\quad - 2\xi(\Delta_{\text{soc}}/\lambda_{\text{R}})(M/\lambda_{\text{R}})] + (9/4)(1 + \xi^2) \\ &\quad + s\sqrt{\{b_{\xi}^2(\delta k, M) - d_{\xi}(\delta k, M)\}}. \end{aligned} \quad (11)$$

Here we have replaced $(3/2)\lambda_{\text{R}}(E)$ in eq. (3) by a scaled-down RSOI, viz. $\lambda_{\text{R}}(E)$, and divided the rest of the terms in the band structure by this redefined RSOI. The band index $\sigma = \pm 1$. We remark that the particle–hole symmetry in (11) is totally unaffected by the dropping of the term $(4\varepsilon c)$ compared to the other terms in the equation $\varepsilon^4 - 2\varepsilon^2 b - 4\varepsilon c + d = 0$. Quite interestingly, the spin polarisation does not become zero in this case as the crucial term in (11),

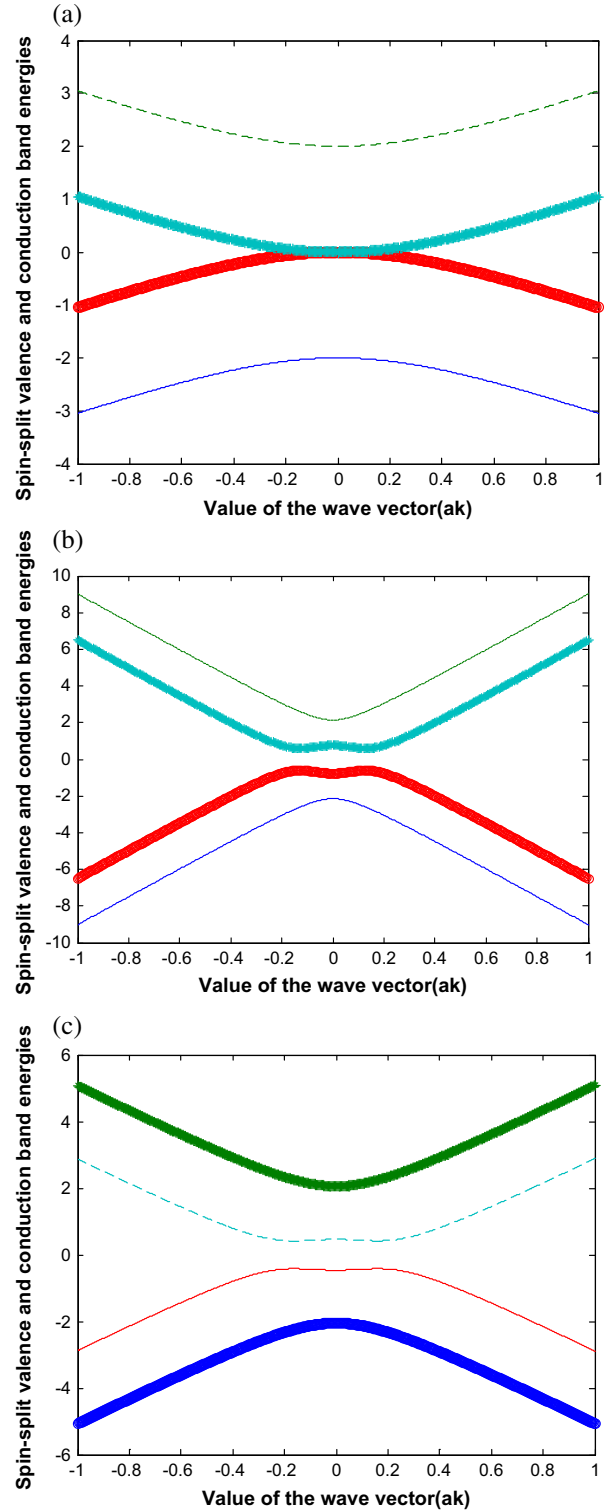


Figure 6. A typical band structure corresponding to a spin-split semimetallic phase of the Tse *et al* [41] model in (12) near the K valley for graphene on WSe_2 and $M = 0$ is in (a). In (b), we have the anticrossing of the non-parabolic bands with opposite spins around \mathbf{K} point for graphene on MoS_2 and $M = 0.10$ meV. In (c), we have band insulator regime where a finite bulk gap develops for MoSe_2 for $M = 0.12$ meV.

viz. $\sqrt{\{b_{\xi}^2(\delta k, M) - d_{\xi}^2(\delta k, M)\}}$ remains real and positive as one can see in figure 5b. When only RSOI and M field are present, the band structure is given by the expression

$$\varepsilon_{\xi,s,\sigma}(\delta k, M) = \sigma[\varepsilon_{\delta k}^2 + (M/\lambda_R)^2 + 2 + 2s\sqrt{\{1 + \varepsilon_{\delta k}^2(1 + (M/\lambda_R)^2)\}}]^{1/2}. \tag{12}$$

This is the same as the spectrum obtained by Tse *et al* [41] and Qiao *et al* [54]. The effective Zeeman field aspect is conspicuous by its absence in the spectrum below as the term $(4\varepsilon c)$ in eq. (6) was ignored in the quartic in ε to obtain a biquadratic. Incidentally, one notices the anticrossing of the non-parabolic bands with opposite spins around \mathbf{K} point for MoS₂ (see figure 6) and other TMDs due to retaining the Rashba spin-orbit coupling and the exchange field only.

4. Discussion

We once again emphasise that the Zeeman term of the spectrum (9), appearing due to the interplay of the substrate-induced interactions with the prime player as the Rashba SOI, is basically due to the presence of the term $(4\varepsilon c)$ in (6) from the analytical viewpoint. This Zeeman field, albeit the Rashba SOI, in conjunction with the intrinsic spin-orbit coupling (SOI), ushers in the spin polarisation. We remark that the above-mentioned fact is a strong enough reason for proceeding with a quartic as we did in eq. (6).

Next we discuss a rather remarkable finding of ours. We have shown the 2D plots of the spin-split conduction and valence band energies for graphene on MoSe₂ at the Dirac points \mathbf{K} and \mathbf{K}' as a function of the dimensionless wave vector ($a|\delta\mathbf{k}|$) for the AA system in figure 7. In figure 7a, at the Dirac points \mathbf{K} for the exchange field

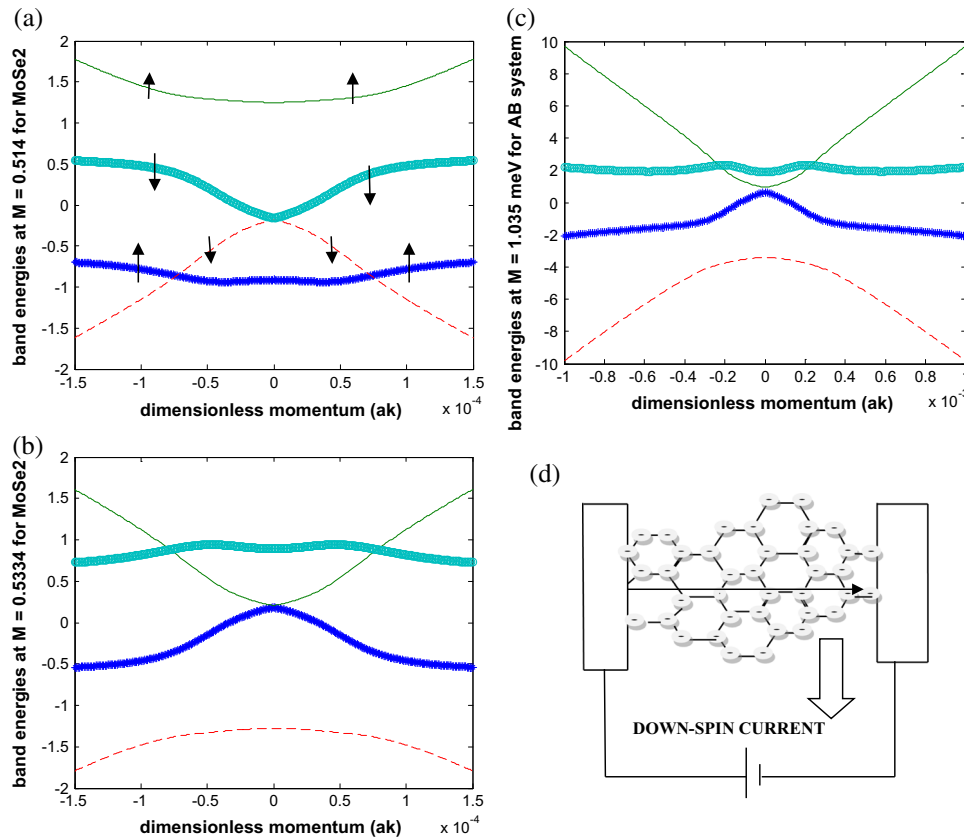


Figure 7. The 2D plots of the spin-split conduction and valence band energies for graphene on MoSe₂ at the Dirac points (DP) \mathbf{K} and \mathbf{K}' as a function of the dimensionless wave vector ($a|\delta\mathbf{k}|$) for the AA system and AB system. In (a), there is gap closing for the spin-down valence band and the spin-down conduction band for the exchange field value equal to 0.514 meV at DP \mathbf{K} . In (b), at the exchange field value equal to 0.5334 meV, there is gap closing for the spin-up valence band and the spin-up conduction band at the Dirac point \mathbf{K}' , while for the spin-down channel the gap remains finite. In (c), a schematic band-gap closing between two bands (valence and conduction bands with up-spin) corresponding to the AB system for graphene in WSe₂ at the Dirac point \mathbf{K} is shown. A trivial band gap at $M < 1$ meV closes at a critical point $M = M_c = 1.035$ meV (half metal). At $M > M_c$ the energy eigenvalues are inadmissible as they become complex. (d) The illustration of a typical spin-filter with AA system.

equal to $M_{c1} = 0.514$ meV, there is a gap closing for the spin-down valence band and the spin-down conduction band, while for the spin-up channel bands the gap remains finite. In figure 7b, at the Dirac points \mathbf{K}' for the exchange field value equal to $M_{c2} = 0.533$ meV, there is a gap closing for the spin-up valence band and the spin-up conduction band. In figure 7c, the gap closing between the valence and the conduction bands with up-spin, corresponding to the AB system for graphene in WSe₂ at the Dirac point \mathbf{K} , has been shown for the exchange field value equal to $M_{c3} = 1.035$ meV. For figures 7a–7d, the trivial band gap at $M < M_c$ closes at a critical point $M = M_c$ (half metal). At $M > M_c$ the energy eigenvalues are inadmissible as they become complex. These findings are expected to pave the way towards possible engineering of graphene spin-filtering by proximity effect. The illustration of a typical spin-filter with AA system operating at $M = M_{c1}$ (half metal) is shown in figure 7d. The down-spin orbits give a conductive nature for the down-spin current, while the up-spin current is almost blocked.

We now put a few words relating to the valley filtering. The idea of the line defect [55–57] has been observed to be useful for a valley filter. The occurrence of line defect in graphene, leading to a pattern of repeated paired pentagons and octagons, was reported by Lahiri [55] for the first time several years ago. Subsequently, Gunlycke and White [39,56] mooted the very promising proposal of scattering-off a line defect to achieve the valley polarisation in graphene. These proposals including the valley polarisation resonator and a detector, however, have not been realised till date due to the extreme difficulty in the experimental implementation.

5. Conclusion

Our broad aim behind the investigation of the effect of the exchange field (M) on the band structure is that, using graphene as a prototypical 2D system, we investigated how material properties change under the influence of the exchange field (M). This is expected to pave the way to the efficient control of spin generation and spin modulation in 2D devices without compromising the delicate material structures. The SO interactions and the exchange field are in the band and do not act as scatterers here. It may be mentioned that inclusion of the exchange field effect in the band is not unprecedented. Introducing in the same manner, Tse *et al* [41] have discussed the evolution of the electronic structure as the exchange field and Rashba SO interaction are introduced to the system.

In conclusion, it may be mentioned that the electrical control of magnetic properties is an important research

goal for low-power write operations in spintronic data storage and logic [57]. The tuning of the exchange field requires similar kind of electrical manipulation of magnetism and magnetic properties in a potential experimental observation of the present effect. In the case of thin films of ferromagnetic semiconductors/insulators, the application of an electric field alters the carrier density which in turn affects the magnetic exchange interaction and the magnetic anisotropy. The magnetic multiferroics, such as BFO, have created quite a stir amongst material research community with the promise of coupling between the magnetic and electric order parameters. A deeper exploration of this coupling needs to be carried out to have access to electrical control of magnetism through the exchange interaction with a ferromagnet. Finally, we believe our results highlight a promising direction for band-gap engineering of graphene.

References

- [1] K S Novoselov, A K Geim, S V Morozov, D Jiang, Y Zhang, S V Dubonos, I V Grigorieva and A A Firsov, *Science* **306**(5696), 666 (2004)
- [2] A H C Neto, F Guinea, N M R Peres, K S Novoselov and A K Geim, *Rev. Mod. Phys.* **81**, 109 (2009)
- [3] I A Ovid'ko, *Rev. Adv. Mater. Sci.* **34**, 1 (2013)
- [4] S A Maier, *Plasmonics: Fundamentals and applications* (Springer, 2007) Chapter 4
- [5] K F Mak, C Lee, J Hone, J Shan and T F Heinz, *Phys. Rev. Lett.* **105**, 136805 (2010)
- [6] B Radisavljevic, A Radenovic, J Brivio, V Giacometti and A Kis, *Nat. Nanotechnol.* **6**, 147 (2011)
- [7] E Gibney, *Nature* **522**, 274 (2015)
- [8] L Likai, Y Yijun, G J Ye, Q Ge, X Ou, H Wu, D Feng, X H Chen and Y Zhang, *Nat. Nanotechnol.* **9**, 372 (2014)
- [9] Geoff Brumfiel, *Nature* **495**, 152 (2013)
- [10] L C Gomes and A Carvalho, *Phys. Rev. B* **92**, 085406 (2015)
- [11] R Guo, X Wang, Y Kuang and B Huang, *Phys. Rev. B* **92**, 115202 (2015)
- [12] A S Rodin, L C Gomes, A Carvalho and A H Castro Neto, *Phys. Rev. B* **93**, 045431 (2016)
- [13] C Kamal, A Chakrabarti and M Ezawa, *Phys. Rev. B* **93**, 125428 (2016)
- [14] A S Rodin, A Carvalho and A H Castro Neto, *Phys. Rev. Lett.* **112**, 176801 (2014)
- [15] E S Reich, *Nature* **506**, 19 (2014)
- [16] J Qiao, *Nat. Commun.* **5**, 4475 (2014)
- [17] L Li, Y Yu, G J Ye, Q Ge, X Ou, H Wu, D Feng, X H Chen and Y Zhang, *Nat. Nanotechnol.* **9**, 372 (2014)
- [18] J Y Tan, A Avsar, J Balakrishnan, G K W Koon, T Taychatanapat, E C T O'Farrell, K Watanabe, T Taniguchi, G Eda, A H Castro Neto and B Özyilmaz, *Appl. Phys. Lett.* **104**, 183504 (2014)

- [19] A K Geim and I V Grigorieva, *Nature* **499**, 419 (2013)
- [20] W Xia, L Dai, P Yu, X Tong, W Song, G Zhang and Z Wang, *Nanoscale* **9**, 4324 (2017)
- [21] L Viti, J Hu, D Coquillat, A Politano, C Consejo, W Knap and M S Vitiello, *Adv. Mater.* **28**, 7390 (2016)
- [22] W J Yu, Z Li, H Zhou, Y Chen, Y Wang, Y Huang and X Duan, *Nat. Mater.* **12**(3), 246 (2013)
- [23] I Leven, T Maaravi, I Azuri, L Kronik and O Hod, *J. Chem. Theory Comput.* **12**(6), 2896 (2016)
- [24] G Argentero, A Mittelberger, M R A Monazam, Y Cao, T J Pennycook, C Mangler, C Kramberger, J Kotakoski, A K Geim and J C Meyer, *Nano Lett.* **17**(3), 1409 (2017)
- [25] M Kindermann, B Uchoa and D L Zero Miller, *Phys. Rev. B* **86**, 115415 (2012)
- [26] M Gmitra, D Kochan, P Hogl and J Fabian, [arXiv:1510.00166](https://arxiv.org/abs/1510.00166) (2015); [arXiv:1506.08954](https://arxiv.org/abs/1506.08954) (2015)
M Gmitra and J Fabian, *Phys. Rev. B* **92**, 155403 (2015)
T Frank, P Hogl, M Gmitra, D Kochan and J Fabian, [arXiv:1707.02124](https://arxiv.org/abs/1707.02124)
- [27] C L Kane and E J Mele, *Phys. Rev. Lett.* **95**, 146802 (2005)
C L Kane and E J Mele, *Phys. Rev. Lett.* **95**, 226801 (2005)
L Fu and C L Kane, *Phys. Rev. B* **76**, 045302 (2007)
- [28] J Balakrishnan, G K W Koon, A Avsar, Y Ho, J H Lee, M Jaiswal, S-J Baeck, J-H Ahn, A Ferreira, M A Cazalilla, A H C Neto and B Ozyilmaz, *Nat. Commun.* **5**, 4748 (2014)
- [29] B A Bernevig and S C Zhang, *Phys. Rev. Lett.* **96**, 106802 (2006)
B A Bernevig, T L Hughes and S C Zhang, *Science* **314**, 1757 (2006)
X-L Qi and S-C Zhang, *Rev. Mod. Phys.* **83**, 1057 (2011)
- [30] Xufeng Kou, Shih-Ting Guo, Yabin Fan, Lei Pan, Murong Lang, Ying Jiang, Qiming Shao, Tianxiao Nie, Koichi Murata, Jianshi Tang, Yong Wang, Liang He, Ting-Kuo Lee, Wei-Li Lee and Kang L Wang, *Phys. Rev. Lett.* **113**, 199901 (2014)
- [31] A J Bestwick, E J Fox, Xufeng Kou, Lei Pan, Kang L Wang and D Goldhaber-Gordon, *Phys. Rev. Lett.* **114**, 187201 (2015)
- [32] S Y Zhou, G-H Gweon, A V Fedorov, P N First, W A de Heer, D-H Lee, F Guinea, A H Castro Neto and A Lanzara, *Nat. Mater.* **6**, 770 (2007)
- [33] D Kochan, S Irmer, M Gmitra and J Fabian, *Phys. Rev. Lett.* **115**, 196601 (2015)
- [34] D Kochan, S Irmer and J Fabian, *Phys. Rev. B* **95**, 165415 (2017)
- [35] Z Wang, D-K Ki, H Chen, H Berger, A H MacDonald and A F Morpurgo, *Nat. Commun.* **6**, 8339 (2015)
- [36] M Daghofer, N Zheng and A Moreo, *Phys. Rev. B* **82**, 121405 RC (2010)
- [37] A M Black-Schaffer, *Phys. Rev. B* **80**, 205416 (2010)
- [38] A Hallal, F Ibrahim, H Yang, S Roche and M Chshiev, *2D Materials* (IOP Publishing Ltd, 2017) Vol 4, No 2
- [39] D Gunlycke and C T White, *Phys. Rev. Lett.* **106**, 13686 (2011)
M M Grujić, M Ž Tadić and F M Peeters, *Phys. Rev. Lett.* **113**, 046601 (2014)
- [40] Q-P Wu, Z-F Liu, A-X Chen, X-B Xiao and Z-M Liu, *Sci. Rep.* **6**, 21590 (2016), <https://doi.org/10.1038/srep21590>
- [41] W-K Tse, Z Qiao, Y Yao, A H MacDonald and Q Niu, *Phys. Rev. B* **83**, 155447 (2011)
- [42] O V Yazye, *Rep. Prog. Phys.* **73**, 056501 (2010)
- [43] Y Yang, Z Xu, L Sheng, B Wang, D Y Xing and D N Sheng, *Phys. Rev. Lett.* **107**, 066602 (2011)
- [44] M Ezawa, *Phys. Rev. Lett.* **109**, 055502 (2012)
- [45] Vo Tien Phong, N R Walet and F Guinea, [arXiv:1707.03868](https://arxiv.org/abs/1707.03868) (2017) (Unpublished)
- [46] A M Alsharari, M M Asmar and S E Ulloa, [arXiv:1608.00992](https://arxiv.org/abs/1608.00992) (2016) (Unpublished)
- [47] Z Wang and S-C Zhang, *Phys. Rev. X* **2**, 031008 (2012)
- [48] M Z Hasan and C L Kane, *Rev. Mod. Phys.* **82**, 3045 (2010)
- [49] X-L Qi and S-C Zhang, *Rev. Mod. Phys.* **83**, 1057 (2011)
- [50] N F Mott, *Proc. R. Soc. London A* **124**, 425 (1929)
- [51] E Burstein, *Phys. Rev.* **93**(3), 632 (1954)
- [52] T S Moss, *Proc. Phys. Soc. B* **67**(10), 775 (1954)
- [53] G I Zebrev, *Proceedings of 26th International Conference on Microelectronics (MIEL)* (Nis, Serbia, 2008), p. 159, [arXiv:1102.2348](https://arxiv.org/abs/1102.2348) (2011)
- [54] Z Qiao, W Ren, H Chen, L Bellaiche, Z Zhang, A H MacDonald and Q Niu, *Phys. Rev. Lett.* **112**, 116404 (2014)
- [55] J Lahiri, *Nat. Nanotechnol.* **5**, 326 (2010)
- [56] D Gunlycke, S Vasudevan and C T White, *Nano Lett.* **13**, 259 (2013)
- [57] S Fusil, V Garcia, A Barthélémy and M Bibes, *Annu. Rev. Mater. Res.* **44**, 91 (2014)